Available online at www.sciencedirect.com
SCIENCE DIRECT
Icarus 182 (2006) 413–423
ICARUS
www.elsevier.com/locate/icarus

First ENA observations at Mars: Subsolar ENA jet

Y. Futaana [a,*], S. Barabash [a], A. Grigoriev [a], M. Holmström [a,b], E. Kallio [c], P. C:son Brandt [d], H. Gunell [a], K. Brinkfeldt [a], R. Lundin [a], H. Andersson [a], M. Yamauchi [a], S. McKenna-Lawler [e], J.D. Winningham [f], R.A. Frahm [f], J.R. Sharber [f], J.R. Scherrer [f], A.J. Coates [g], D.R. Linder [g], D.O. Kataria [g], T. Säles [c], P. Riihelä [c], W. Schmidt [c], H. Koskinen [h], J. Kozyra [i], J. Luhmann [j], E. Roelof [c], D. Williams [c], S. Livi [c], C.C. Curtis [k], K.C. Hsieh [k], B.R. Sandel [k], M. Grande [l], M. Carter [l], J.-A. Sauvaud [m], A. Fedorov [m], J.-J. Thocaven [m], S. Orsini [n], R. Cerulli-Irelli [n], M. Maggi [n], P. Wurz [o], P. Bochsler [o], N. Krupp [p], J. Woch [p], M. Fränz [p], K. Asamura [q], C. Dierker [r]

[a] *Swedish Institute of Space Physics, Box 812, SE-981 28 Kiruna, Sweden*
[b] *NASA Goddard Space Flight Center, Greenbelt, MD 20771, USA*
[c] *Finnish Meteorological Institute, Box 503, FIN-00101 Helsinki, Finland*
[d] *Applied Physics Laboratory, Johns Hopkins University, Laurel, MD 20723-6099, USA*
[e] *Space Technology Ireland, National University of Ireland, Maynooth, Co. Kildare, Ireland*
[f] *Southwest Research Institute, San Antonio, TX 7228-0510, USA*
[g] *Mullard Space Science Laboratory, University College London, Surrey RH5 6NT, UK*
[h] *Department of Physical Sciences, University of Helsinki, P.O. Box 64, 00014 Helsinki, Finland*
[i] *Space Physics Research Laboratory, University of Michigan, Ann Arbor, MI 48109-2143, USA*
[j] *Space Science Laboratory, University of California in Berkeley, Berkeley, CA 94720-7450, USA*
[k] *University of Arizona, Tucson, AZ 85721, USA*
[l] *Rutherford Appleton Laboratory, Chilton, Didcot, Oxfordshire OX11 0QX, UK*
[m] *Centre d'Etude Spatiale des Rayonnements, BP-4346, F-31028 Toulouse, France*
[n] *Istituto di Fisica dello Spazio Interplanetari, I-00133 Rome, Italy*
[o] *Physikalisches Institut, University of Bern, CH-3012 Bern, Switzerland*
[p] *Max-Planck-Institut für Aeronomie, D-37191 Katlenburg-Lindau, Germany*
[q] *Institute of Space and Astronautical Science, 3-1-1 Yoshinodai, Sagamihara, Japan*
[r] *Technical University of Braunschweig, Hans-Sommer-Strasse 66, D-38106 Braunschweig, Germany*

Received 16 April 2005; revised 10 August 2005

Available online 26 January 2006

Abstract

The Neutral Particle Detector (NPD), an Energetic Neutral Atom (ENA) sensor of the Analyzer of Space Plasmas and Energetic Atoms (ASPERA-3) on board Mars Express, detected intense fluxes of ENAs emitted from the subsolar region of Mars. The typical ENA fluxes are $(4–7) \times 10^5$ cm^{-2} sr^{-1} s^{-1} in the energy range 0.3–3 keV. These ENAs are likely to be generated in the subsolar region of the martian exosphere. As the satellite moved away from Mars, the ENA flux decreased while the field of view of the NPD pointed toward the subsolar region. These decreases occurred very quickly with a time scale of a few tens of seconds in two thirds of the orbits. Such a behavior can be explained by the spacecraft crossing a spatially constrained ENA jet, i.e., a highly directional ENA emission from a compact region of the subsolar exosphere. This ENA jet is highly possible to be emitted conically from the subsolar region. Such directional ENAs can result from the anisotropic solar wind flow around the subsolar region, but this can not be explained in the frame of MHD models.

Keywords: Mars, atmosphere; Solar wind; Magnetospheres

* Corresponding author. Fax: +46 980 79091.
E-mail address: futaana@irf.se (Y. Futaana).

0019-1035/$ – see front matter
doi:10.1016/j.icarus.2005.08.024

1. Introduction

Energetic neutral atom (ENA) imaging has become one of the standard ways to infer the interaction between neutral particles and space plasma. Since ENAs are not affected by the electromagnetic field, ENA imaging is a powerful diagnostic tool to investigate plasma characteristics remotely.

High energy neutral atoms (>10 keV) emitted from the terrestrial ring current have been detected by charged particle detectors (e.g., Roelof et al., 1985; Voss et al., 1993). The first dedicated ENA instrument was carried by the Astrid-1 satellite (Barabash, 1995). After that, a number of missions carried out ENA measurements in space to investigate dynamics of the terrestrial ionosphere and the magnetosphere (e.g., Barabash et al., 1998; C:son Brandt et al., 2001). The IMAGE mission carries three ENA imagers so as to cover a wide energy range, namely High Energy Neutral Atoms (HENA), Medium Energy Neutral Atoms (MENA), and Low Energy Neutral Atoms (LENA). The HENA imager, which detects ENAs in an energy range 10–500 keV, is designed to investigate the ring current, the inner plasmasheet and the substorm injection boundary (Mitchell et al., 2000). The MENA imager can measure ENAs with energies of 1–30 keV to image the ion populations of the cusp in addition to the ring current, near-Earth plasmasheet and the nightside injection boundary (Pollock et al., 2000). The LENA imager can detect ENAs in the energy range 10–500 eV. LENA is designed to image the outflow of low energy ions from the auroral ionosphere (Moore et al., 2000).

The ENA imaging technique has also been applied to planetary missions. Cassini carries an ENA instrument named the Magnetosphere Imaging Instrument, Ion and Neutral Camera (MIMI/INCA), to Saturn. Mauk et al. (2003) analyzed ENA images obtained in the vicinity of Jupiter while en route to Saturn, and found that Europa unexpectedly generates a gas cloud comparable to the gas content associated with the volcanic Io.

The ESA martian mission, Mars Express, carries a plasma and neutral particle package, Analyzer of Space Plasma and Energetic Atoms (ASPERA-3). ASPERA-3 comprises four instruments: two ENA sensors, an electron spectrometer and an ion analyzer (Barabash et al., 2004). The two ENA sensors are the Neutral Particle Imager (NPI) and the Neutral Particle Detector (NPD). The NPI is designed to measure ENAs with a relatively high angular resolution of $4.5^\circ \times 11.25^\circ$, but with no mass and energy analysis. The NPD can resolve particle velocities and masses but has a lower angular resolution ($\sim 5^\circ \times 40^\circ$).

The martian plasma environment is much different from that of the Earth. Magnetic field observations by Mars-2, -3, and -5 spacecraft revealed that Mars does not have a strong intrinsic magnetic field (Dolginov et al., 1973; Dolginov, 1978). The Mars Global Surveyor confirmed that there are no intrinsic magnetic field, while there exist strongly magnetized regions (Acuña et al., 1998).

Due to the lack of the global magnetic field, the solar wind can enter the region of high neutral gas density. Therefore, generation of intense ENA fluxes through the charge-exchange mechanism can take place everywhere in the near-Mars space. Candidates for ENA generation around Mars are suggested by several numerical simulations as follows: the supersonic solar wind (Holmström et al., 2002), the shocked solar wind (Holmström et al., 2002), accelerated planetary ions (Barabash et al., 2002; Lichtenegger et al., 2002), solar wind protons neutralized by the charge exchange with the tiny Phobos atmosphere (Mura et al., 2002), atmospheric atoms sputtered by picked-up O^+ ions (Luhmann and Bauer, 1992), and solar wind protons backscattered from the martian exosphere (Kallio and Barabash, 2001; Holmström et al., 2002).

In the present study, we focus on ENAs generated at the subsolar region of Mars. Only NPD data are used in this analysis. The NPD detected intense fluxes when its fields of view looked at the subsolar region. In Section 2, we describe the NPD instrument. In Section 3, we present two typical NPD observations of the intense fluxes emanating from the subsolar region. In Section 4, the origin and the generation mechanism of those ENAs are discussed.

2. Instrumentation and data

The NPD sensor consists of two identical detectors, NPD-1 and NPD-2. The only difference between them is the direction of their fields of view. The NPD measures ENA differential fluxes over the energy range 100 eV to 10 keV while resolving H and O. Each detector has a $9^\circ \times 90^\circ$ intrinsic field of view divided into three pixels (Dirs-0, -1, and -2). The angular resolution per single pixel is $\sim 5^\circ \times 40^\circ$ (full width at half maximum). This means that a slight overlap of viewing angles exists. Fig. 1 shows a schematic view of the NPD configuration and viewing directions relative to the spacecraft body.

ENAs entering the sensor through a pin hole first hit a start surface at a shallow angle of 20°. Each impact produces secondary electrons, which are transported to an MCP (Microchannel Plate) assembly giving a START signal. An electrostatic deflector to remove charged particles is placed in front of the pin hole. The incident ENAs that hit the start surface are reflected and they are carried toward stop surfaces, where secondary electrons are newly generated to give a STOP signal. There are three stop surfaces, which correspond to the direction of the incident ENAs. By taking one-by-one coincidences of the START and STOP signals within a certain window, the time-of-flight (TOF) of the particles can be obtained. The TOF is converted into velocity using the fixed 8-cm distance between the start and stop surfaces. To obtain the original velocity, the measured velocity must be corrected for a 34% energy loss during the ENA-start surface interaction. The pulse-height (PH) distribution analysis of the STOP signals provides a rough determination of ENA mass. The geometrical factor (G_0) and the efficiency (ϵ) is obtained from ground calibrations and the product of these quantities is $\epsilon \cdot G_0 \sim (9.78\text{–}17.1) \times 10^{-5}$ cm^2 sr for 0.7–1.3 keV hydrogen atoms.

The NPD sensor is an open system, and thus UV photons entering the instrument results in non-correlated counts on START and STOP systems. The non-correlated count rates on START is ~10 kHz and on each STOP ~300 Hz. These non-correlated signals result in random correlated TOF signal as a background level. Since the TOF distribution of this signal is basically con-

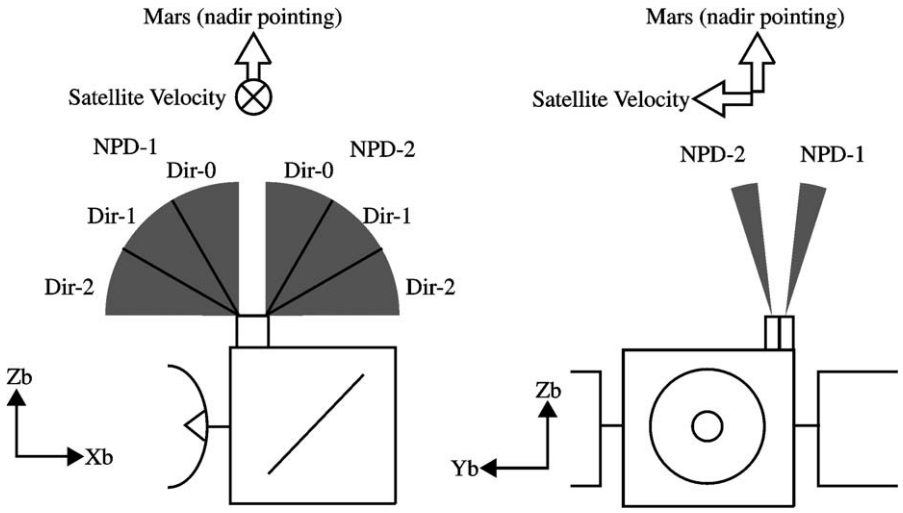

Fig. 1. The configuration of the NPD instruments on board Mars Express seen from (left) the $-Y_b$-direction and (right) the $-X_b$-direction. The satellite coordinate system is used. Two NPD instruments are mounted on the Z_b-plane and each has a $9^\circ \times 90^\circ$ field of view. The field of view inclines $\mp 15^\circ$ in the Y_b-direction for NPD-1 and NPD-2, respectively. The attitude mode of the satellite during the observations discussed in this paper was nadir pointing, i.e., Z_b pointed toward the center of Mars.

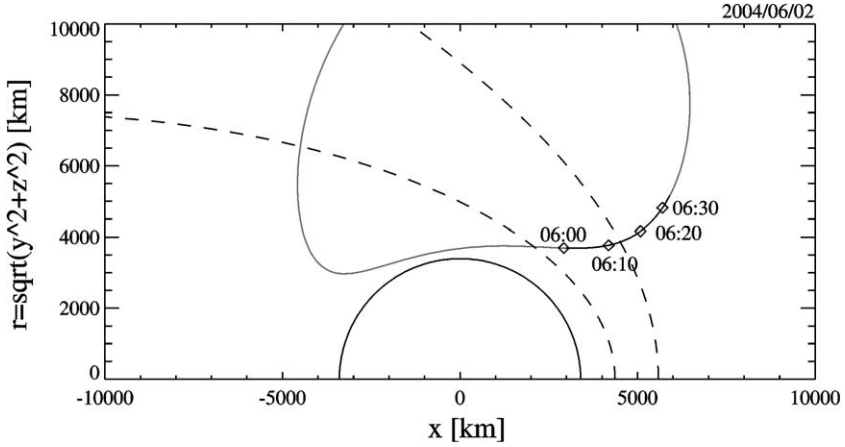

Fig. 2. The Mars Express trajectory on June 2, 2004 (Orbit 466) in the cylindrical coordinate system: the horizontal axis corresponds to the x-direction of the MSO coordinates and the vertical axis is the distance from the Mars–Sun line. The dashed lines are the modeled bow shock and magnetic pile-up boundary (Vignes et al., 2000).

stant over the entire TOF window, we can estimate the background level from the TOF spectrum. For absolute flux calculation, this random correlated signal must be subtracted from the recorded signal.

In this study, we use data recorded between May 24 and July 1, 2004, when the orbit and the attitude of Mars Express were optimal to investigate ENA emissions from the subsolar region. The NPD operations last ~30 min, starting ~20 min after the periapsis. During these time intervals, Mars Express was nadir pointing, which means that the plane on which NPD is mounted ($+Z_b$-plane in Fig. 1) faced the martian surface, and the symmetry axis between DIR-0 of NPD-1 and NPD-2 (the Z_b-axis) pointed toward the center of Mars.

During the observations, the NPD was running in so-called 'binning-matrix' mode. In this mode, individual coincident counts are accumulated in logarithmically divided 16 TOF bins and in 1, 2, or 16 PH bins (depending on a submode). The advantage of the binning-matrix mode is its relatively high time resolution (1 s) but a disadvantage is the coarse TOF resolution (16 steps over 50–1900 ns). The TOF spectra observed by NPD-1 are used in this study since NPD-2 did not view toward the subsolar region.

3. Observation

Fig. 2 shows the Mars Express trajectory on June 2, 2004 (Orbit 466) in the cylindrical coordinate system, based on the Mars–Sun orbit (MSO) coordinate system, in which the x-axis is aligned from Mars to the Sun, z-axis is perpendicular to the martian orbital plane and the y-axis completes the right-handed system. In the cylindrical coordinate system, the horizontal axis corresponds to the x-direction of the MSO coordinates, and the vertical axis is the distance from the Mars–Sun line ($r = \sqrt{y^2 + z^2}$). The pericenter height is 265 km (05:40 UT). The NPD operated between 06:03 and 06:31 UT. Mars Express was located in the magnetosheath region at the start of the op-

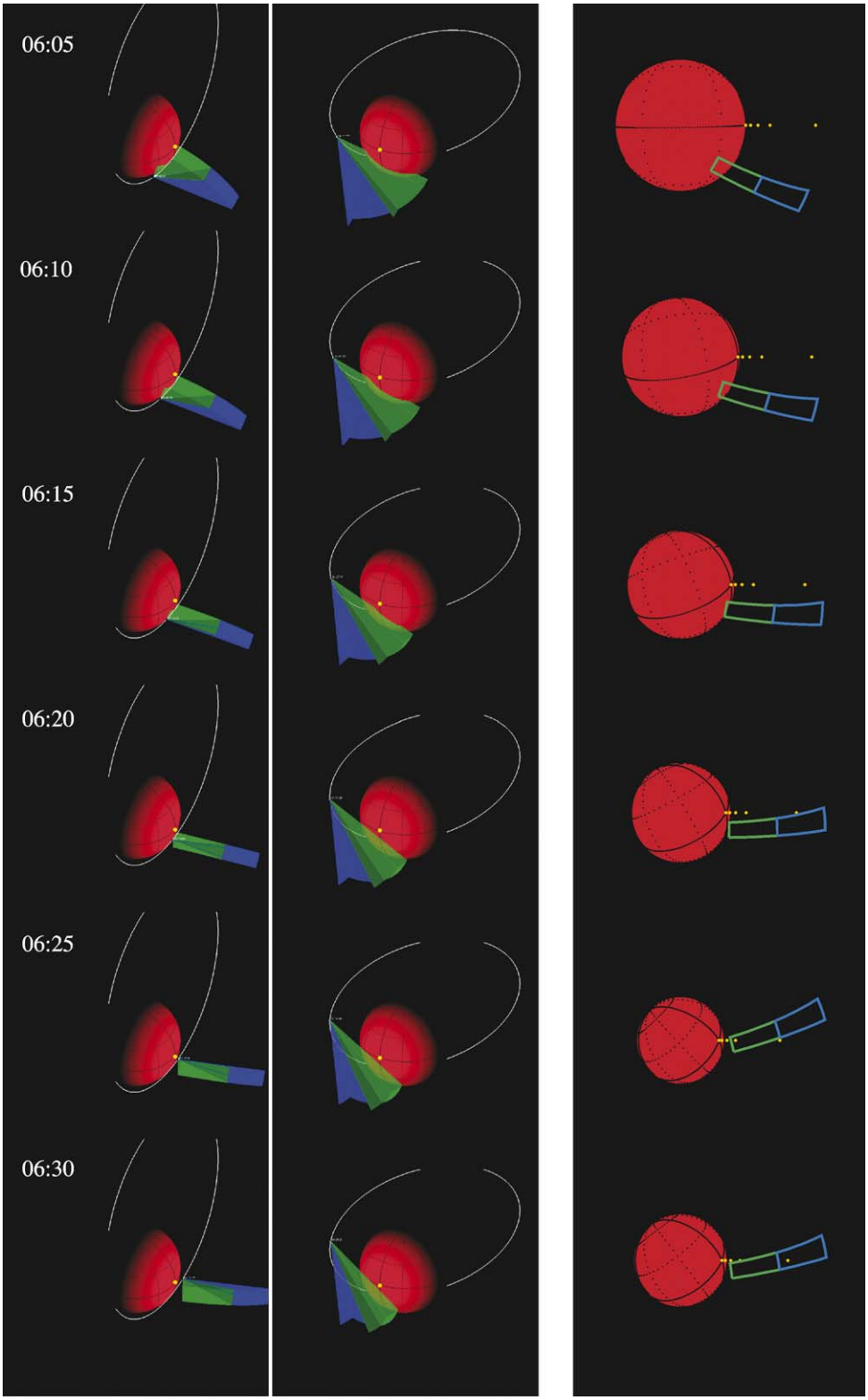

Fig. 3. The viewing geometry on June 2, 2004. The first and second columns are 3-D representations of the NPD-1 FOV at different times seen from different view points. The green and blue fans are the DIR-1 and DIR-2 FOVs, respectively. The third column is a fish-eye projection of the same geometry (see text). The red circle represents Mars and the green and blue rectangles show the DIR-1 and DIR-2 FOVs, respectively. The yellow dots are the directions toward points of 200, 500, 1000, and 3397 km (=1 R_m) above the subsolar point.

erations, and moved to the solar wind region after a bow shock crossing at 06:05 UT as deduced from data recorded by the ASPERA-3 ion (IMA) and electron (ELS) sensors.

The viewing geometry of the NPD-1 is shown in Fig. 3. The first and second columns are 3-D representations of the NPD-1 fields of view (FOV) at different times along the Mars Express

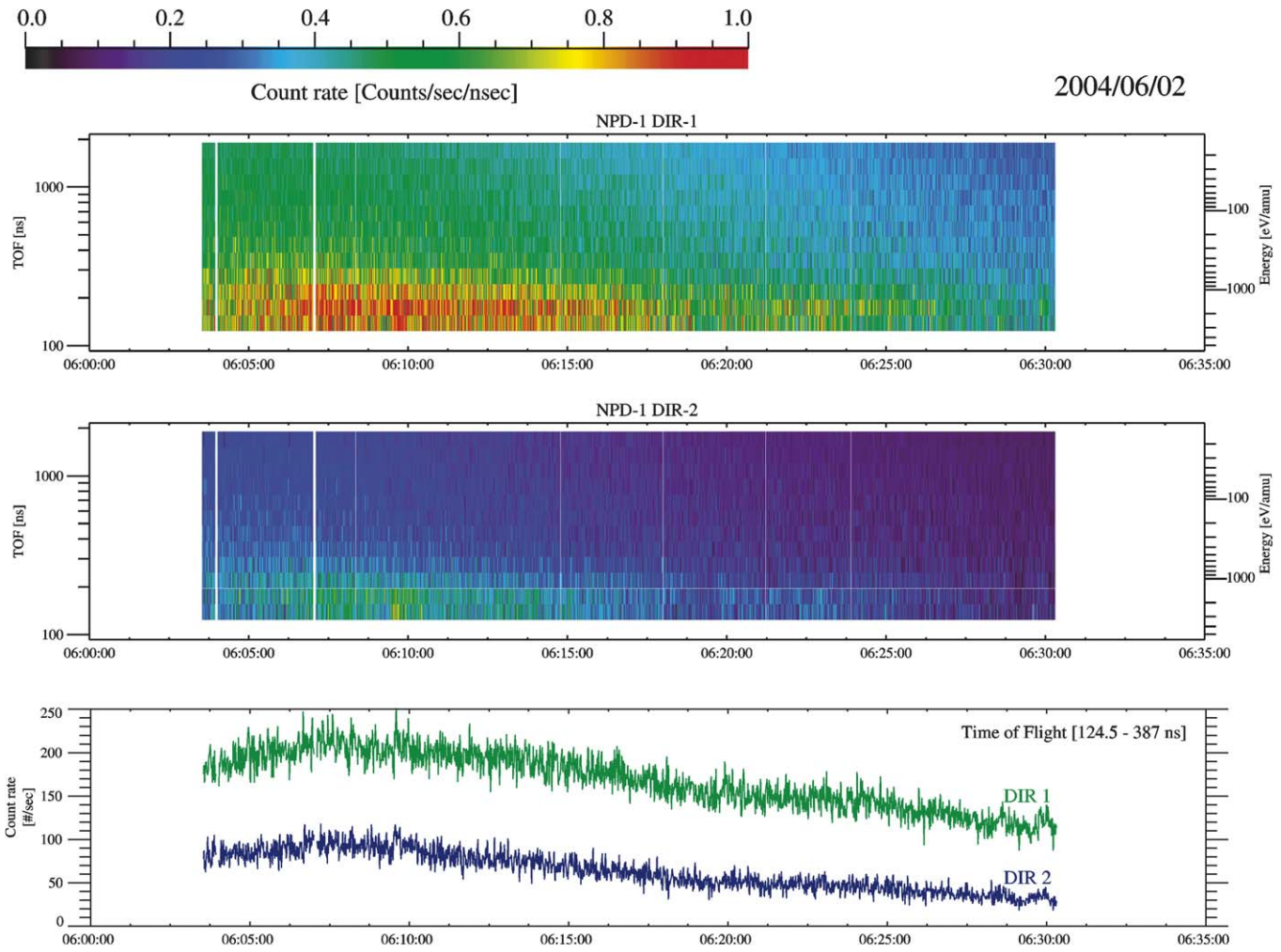

Fig. 4. NPD measurements between 06:03 and 06:31 UT on June 2, 2004. The first and second panels are TOF spectrograms of DIR-1 and DIR-2, respectively. The right axis gives the corresponding energy per mass. The third panel shows the count rates of DIR-1 and DIR-2 integrated over the TOF range of 124.5–387 ns (0.22–2.2 keV/amu).

orbit (white ellipse) seen from different view points. The green and blue fans are the DIR-1 and DIR-2 FOVs and the yellow dots correspond to the subsolar point. The third column is a fish-eye projection of the same geometry, i.e., an image as it would be seen by an observer located on the spacecraft with the boresight direction aligned toward the nadir. The red circle represents Mars and the green and blue rectangles show the DIR-1 and DIR-2 FOVs, respectively. The yellow dots indicate the directions toward points of 200, 500, 1000, and 3397 km (=1 R_m) above the subsolar point.

Fig. 4 shows measurements from the NPD-1 sensor. The first and second panels are TOF spectrograms of DIR-1 and DIR-2, respectively. The right axis gives the corresponding energy per mass. Intense ENA signals with TOF less than 400 ns, corresponding to ∼200 eV/amu. The third panel shows the count rate of DIR-1 and DIR-2 integrated over the TOF from 124.5 to 387 ns, which corresponds to the energy range 0.34–3.2 keV/amu.

Fig. 5 shows the TOF spectra of NPD-1/DIR-1 averaged over the time periods 06:10–06:15 and 06:25–06:30 UT on June 2, 2004. The peak appears at the energy of ∼1.5 keV/amu.

The total ENA count rate decreased as the spacecraft moved away from Mars (Fig. 4). As seen in Fig. 3, the FOVs of NPD-1/DIR-1 and DIR-2 covered the subsolar region during the observations.

The typical integrated count rate was ∼200 counts/s (Fig. 4). The random correlated count (a background level; see Section 2), is estimated to be ∼0.48 counts/s per 1-ns bin from the spectrum (the dashed line in Fig. 5), which corresponds to ∼130 counts/s in TOF range 124.5–387 ns. Then, the effective ENA signal is ∼70 counts/s. Using the geometrical factor of the instrument ($G_0 \cdot \epsilon \sim (9.78–17.1) \times 10^{-5}$ cm^2 sr for 0.7–1.3 keV hydrogen atoms), the ENA differential flux, J, is calculated as $J = (4–7) \times 10^5$ cm^{-2} sr^{-1} s^{-1}, assuming the observed ENAs are hydrogen.

We now show another example of an NPD observation. The observation was conducted on May 30, 2004. The orbit and the FOVs are shown in Figs. 6 and 7, respectively. They are almost the same as in the previous example of June 2. Fig. 8 shows the NPD-1 measurement. Instead of a gradual decrease of the count rate as in the previous example, the NPD observed a sharp decrease in the count rate at ∼11:03 UT within a time scale of

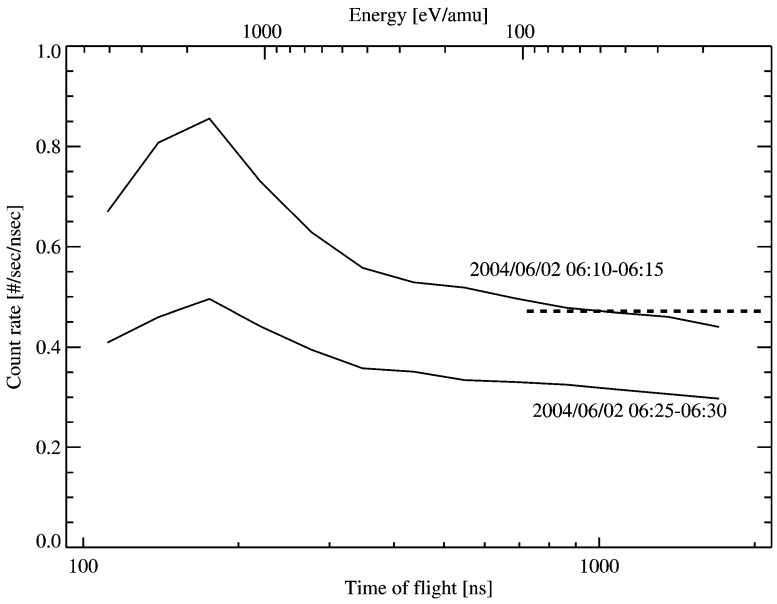

Fig. 5. TOF spectra of NPD-1/DIR-1 obtained during the time period 06:10–06:15 and 06:25–06:30 on June 2, 2004. The dashed line, 0.48 counts/s per 1-ns bin, depicts the background level of the period 06:10–06:15.

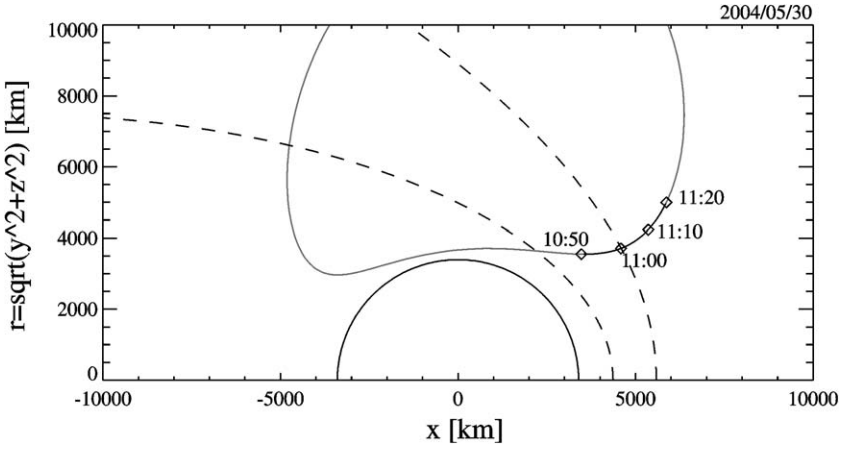

Fig. 6. The trajectory of the Mars Express (Orbit 456) in the same format as in Fig. 2.

the order of 1 min. Fig. 9 shows the TOF spectra at 10:56–11:00 (before the decrease) and at 11:12–11:16 (after the decrease). Their shapes are very similar to those obtained on 2nd June (Fig. 5).

Another characteristic signature is a short bursty enhancement with patch-like increases in the ENA count rate, observed at around 11:10 UT. Since the FOV pointed at the subsolar region and the TOF spectrum of these enhanced ENAs was almost the same as that observed before the sharp decrease, they probably originated from the same source.

We searched through all of the TOF spectrograms obtained by the NPD-1 between May 24, 2004 and July 1, 2004, when the trajectories and the attitude of Mars Express were nearly the same, which means that the FOVs of the NPD-1 are almost the same. A total of 38 orbits were available, and the NPD observed the intense ENA flux 36 of these orbits. We used all the TOF spectrograms such as Figs. 4 and 8 to divide the observations into two categories above. The sharp changes in ENA flux were observed in 23 orbits (64%), and the gradual decrease (i.e., no sudden change of the ENA flux) was seen in 13 orbits (36%).

4. Discussion

The NPD detected intense ENA fluxes with energies in the range 0.3–3 keV/amu when the FOVs of the NPD pointed toward the subsolar exosphere. We will next discuss the source region and the source mechanism.

From the FOV configurations, three of the six known mechanisms listed in Section 1 are not possible to explain the ENA flux: solar wind ENAs, sputtered ENAs by picked up ions and Phobos-related ENAs. And then, the following three known mechanisms may explain the NPD observations: solar wind protons and ENAs backscattered from the martian exosphere (Kallio and Barabash, 2001), shocked solar wind protons neutralized by the martian hydrogen corona (Holmström et al., 2002), and accelerated planetary ions (Lichtenegger et al.,

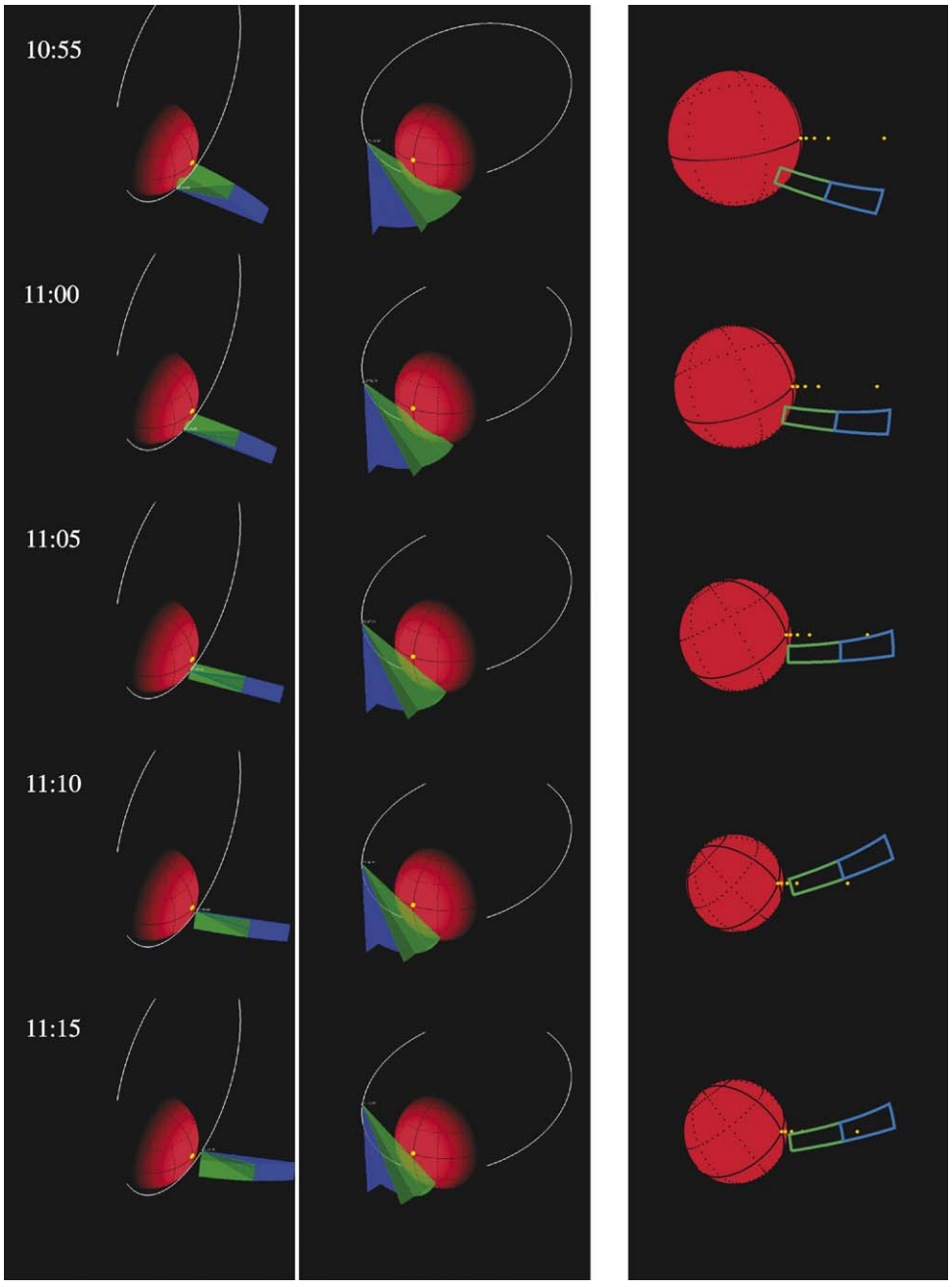

Fig. 7. The viewing geometry on May 30, 2004. The format is the same as in Fig. 3.

2002). These processes are all related to interactions between the solar wind and the martian upper atmosphere, and the ENA generation is expected to be large in the subsolar region because the solar wind can penetrate to much lower altitudes, where a dense neutral atmosphere exists.

One of the most important results from the NPD observations is that the ENA flux depends highly on the position of the satellite, even though the FOVs of the NPD were always viewing toward the subsolar region. This observational fact can be explained in terms of a highly directional ENA emission around the subsolar region, i.e., a subsolar ENA jet. Fig. 10 presents a schematic representation of the concept of a subsolar ENA jet. Such an ENA flux can be detected when the sensor is within this ENA jet (for case (a) in the figure). As soon as the spacecraft leaves the jet (case (b) in the figure), the ENAs cannot be detected even if the instrument FOV covers the source region.

One question is how such an ENA jet can be generated around the subsolar region. Since backscattered ENAs are expected to be emitted isotropically from the martian upper atmosphere (Kallio and Barabash, 2001; Futaana et al., 2006), the following two mechanisms are likely candidates: shocked solar wind and accelerated planetary ions. Both can potentially generate the subsolar ENA jet implied by the NPD observations.

First, we consider the shocked solar wind just above the induced magnetosphere boundary (IMB), which is defined as the envelope of the martian magnetosphere, i.e., the stopping

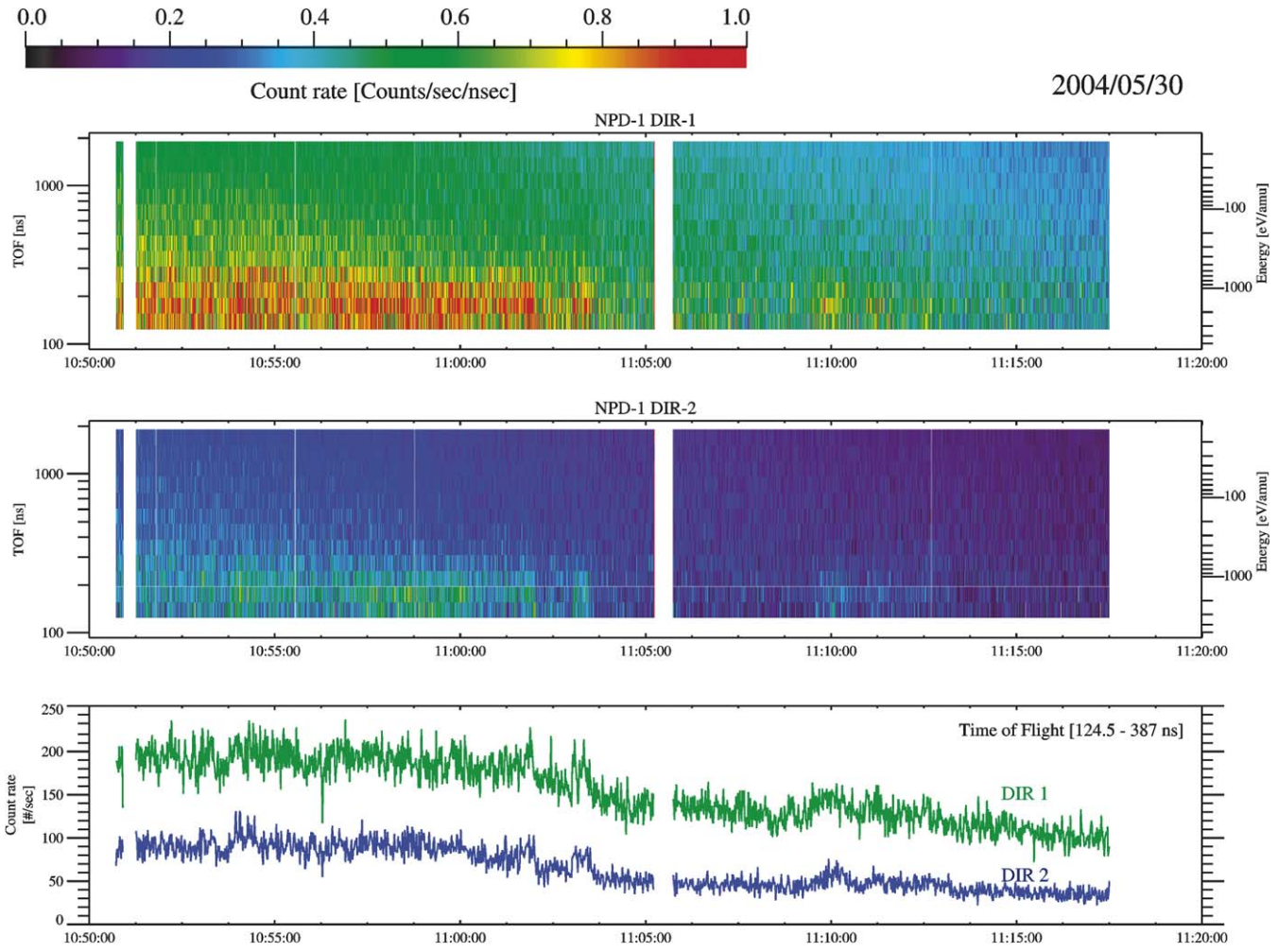

Fig. 8. NPD measurements recorded between 10:51 and 11:18 UT on May 30, 2004. The format is the same as in Fig. 4.

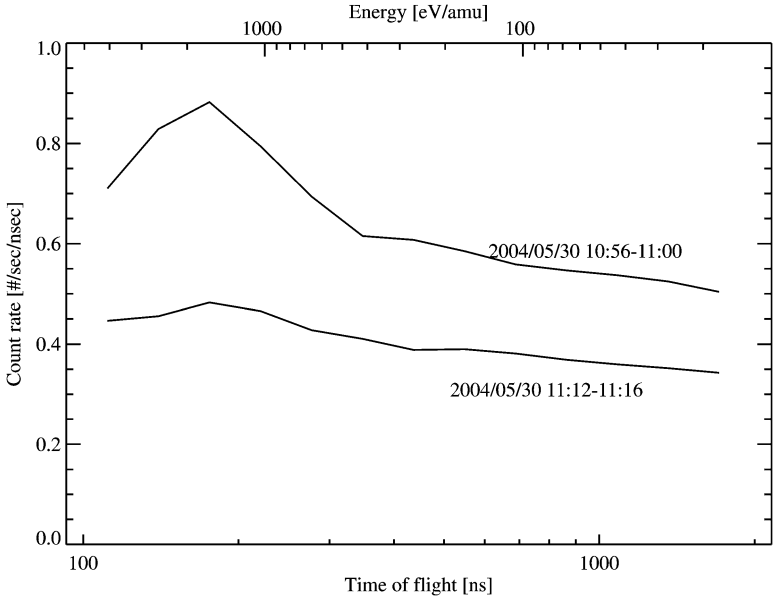

Fig. 9. TOF spectra of NPD-1/DIR-1 averaged over the time interval 10:56–11:00 and 11:12–11:16 on May 30, 2004.

boundary of the solar wind (Lundin et al., 2004), at the subsolar region. There, the stream line of the shocked solar wind is highly deflected, and an ENA jet can be formed by charge exchanges with the dense atmosphere. This scenario is possible

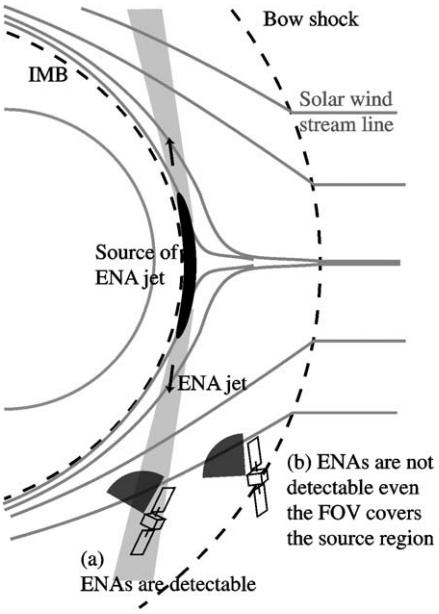

Fig. 10. Geometry of the subsolar ENA jet. The subsolar jet can be detected when the sensor is within it (case (a)). As soon as the spacecraft leaves the jet (case (b)) the ENAs can not be detected even though the instrument FOV covers the source region.

because the solar wind can actually reach altitudes as low as 300 km in the subsolar region, as evidenced by recent results of ASPERA-3 ion mass spectrometer (Lundin et al., 2004). The size of the source must be an order of the scale height of the hydrogen, that is several hundred kilometers. ENA production from the shocked solar wind is described in Kallio and Barabash (2001) and Holmström et al. (2002) in more detail. However, the model has a singularity at the subsolar point, and can not be used to simulate ENA productions there, while the ENA generation must be the highest in the subsolar region.

Second, we mention accelerated planetary protons that are converted to ENAs through the charge-exchange process (see discussion of Lichtenegger et al., 2002). Planetary protons transported to the magnetosheath are accelerated by the electromagnetic field, and would have approximately the same velocity as the ambient shocked solar wind. Such accelerated protons can form an ENA jet after the experience of charge exchanges. Lichtenegger et al. (2002) concluded that the ENA flux produced by this mechanism would be as high as the shocked solar wind ENAs. These authors also compared the energy spectra of these two mechanisms, and concluded that careful analysis of the spectra can distinguish the accelerated planetary ENAs from the shocked solar wind ENAs. Actually, it is difficult in the present instance to discuss the spectra in detail because they are too coarse due to the observation mode employed.

Note that the above two mechanisms are highly related. Around the IMB, the shocked solar wind flow accelerate the planetary ions, and one of the generation of the planetary ions is the charge-exchange mechanism between the shocked solar wind protons and the exospheric hydrogen atoms. The generation region and the directionality for the above two mechanisms are almost the same. The major difference is the source of ENAs, i.e., the shocked solar wind or the planetary ions.

The observation geometry over all 38 events was rather similar in the MSO coordinate system. During the observations, the NPD field of view plane was close to the ecliptic plane. Therefore, only limited range of angle ($<30°$) relative to the ecliptic plane was sampled and we cannot conclude whether we can consider the ENA jet as the conical ENA emission, i.e., whether the ENA emission is cylindrically symmetric or not. Existing MHD models (e.g., Tanaka and Murawski, 1997) of the solar wind–Mars interaction provide rather cylindrically symmetric pattern of the solar wind proton flow around the Mars, and thus one would be in favor of the conical ENA jet. More precise hybrid models (e.g., Brecht, 1997) show asymmetric features of the proton flow in association with the interplanetary electric field direction ($E = -V_{SW} \times B_{IMF}$, where V_{SW} and B_{IMF} are the solar wind velocity and the interplanetary magnetic field, respectively). The analysis has not been taken the electromagnetic direction into account because of the absence of the magnetometer aboard Mars Express. However, since the observations cover long period (∼40 days), the distribution of the IMF directions can be considered to be random. Therefore, the conical ENA jet geometry is rather plausible, and Fig. 10 is considered as a cut of the axi-symmetric geometry of the conical ENA jet.

The NPD observations show another significant result. The ENA count rate was found to decrease very rapidly (∼several tens of seconds) in two thirds of the orbits, as shown in Fig. 8. This implies that the source of the ENA jet should be confined in space. We do not have a clear explanation as to what controls its size and directionality. One possibility concerns the upstream conditions, such as the solar wind density, velocity and temperature. These parameters control global structures of the martian plasma environment, so that the properties of the ENA jet are also modified. The anisotropy of the global plasma environment is another possible agent. As is pointed out by many authors (e.g., Terada et al., 2002), the plasma environment are highly anisotropic in association with the direction of the convectional electric field.

Existence of such compact and directional ENA jet also raises a question with regard to the validity of current MHD models. In all MHD models, the subsolar point is a stagnation point with almost zero bulk velocity. The associated ENA emissions should be rather isotropic due to the high temperature of shocked solar wind. However, the observations indicate highly anisotropic emission with solar wind energy. MHD models may not be valid in describing the martian subsolar region because the system size is comparable to the proton gyroradius. Therefore, one needs more detailed 3-D hybrid models dedicated particularly to this domain in order to investigate the physics of the sharp decrease of the ENA signal.

What causes the short bursty enhancements in the ENA signal such as were observed at 11:10 UT, May 30 (Fig. 8)? A possibility is the temporal changes in the upstream conditions, e.g., the magnetic field intensity and direction, the solar wind density, velocity and temperature (Holmström et al., 2002). Note that these ENA bursts can not be explained by changes in the observational geometry, which remained the same during the observation.

5. Summary

The NPD, an ENA sensor of the ASPERA-3 experiment on board Mars Express, detected intense fluxes of ENAs emitted from the subsolar exosphere. Typical ENA fluxes were (4–7) $\times 10^5$ $cm^{-2}\,sr^{-1}\,s^{-1}$ in the energy range of 0.3–3 keV/amu. These ENAs are likely to be generated through charge exchange between the shocked solar wind protons and the martian exosphere in the subsolar region, where the solar wind plasma penetrate to its lowest altitude and where the neutral gas density is high.

As the satellite moved away from Mars, the observed ENA signal decreased as long as the FOVs of the NPD pointed at the subsolar region. These decreases are gradual in one third of the orbits, while the decreases are very sharp (on a scale of a few tens of seconds) in two thirds of the orbits. This behavior can be explained if the spacecraft crossed a spatially constrained ENA jet, as shown in Fig. 10. Such anisotropic ENAs indicate that the solar wind flow around the subsolar region is also highly anisotropic, and this can not be explained in the frame of MHD models.

Acknowledgments

The ASPERA-3 experiment on the European Space Agency (ESA) Mars Express is a joint effort by 15 laboratories in 10 countries, all supported by their national agencies. We thank all these agencies, as well as the various departments and institutes hosting these efforts. Y. Futaana is supported by Postdoctoral Fellowships for Research Abroad of the Japan Society for the Promotion Science.

References

Acuña, M.H., Connerney, J.E.P., Wasilewski, P., Lin, R.P., Anderson, K.A., Carlson, C.W., McFadden, J., Curtis, D.W., Mitchell, D., Reme, H., Mazelle, C., Sauvaud, J.A., d'Uston, C., Cros, A., Medale, J.L., Bauer, S.J., Cloutier, P., Mayhew, M., Winterhalter, D., Ness, N.F., 1998. Magnetic field and plasma observations at Mars: Initial results of the Mars Global Surveyor mission. Science 279, 1676–1680.

Barabash, S., 1995. Satellite observations of the plasma–neutral coupling near Mars and the Earth. Ph.D. thesis, Swedish Institute of Space Physics.

Barabash, S., Norberg, O., Lundin, R., Olsen, S., Lundin, K., Brandt, P.C., Roelof, E.C., Chase, C.J., Mauk, B.H., Koskinen, H., Rynö, J., 1998. Energetic neutral atom imager on the Swedish microsatellite Astrid. In: Pfaff, R.F., Borovsky, J.E., Young, D.T. (Eds.), Measurement Techniques in Space Plasmas, Field. Am. Geophys. Union, Washington, DC, pp. 257–262. AGU Geophysical Monograph 103.

Barabash, S., Holmström, M., Lukyanov, A., Kallio, E., 2002. Energetic neutral atoms at Mars. 4. Imaging of planetary oxygen. J. Geophys. Res. 107 (A10), doi:10.1029/2001JA000326. 1280.

Barabash, S., Lundin, R., Andersson, H., Gimholt, J., Holmström, M., Norberg, O., Yamauchi, M., Asamura, K., Coates, A.J., Linder, D.R., Kataria, D.O., Curtis, C.C., Hsieh, K.C., Sandel, B.R., Fedorov, A., Grigoriev, A., Budnik, E., Grande, M., Carter, M., Reading, D.H., Koskinen, H., Kallio, E., Riihela, P., Säles, T., Kozyra, J., Krupp, N., Livi, S., Woch, J., Luhmann, J., McKenna-Lawlor, S., Orsini, S., Cerulli-Irelli, R., Maggi, M., Morbidini, A., Mura, A., Milillo, A., Roelof, E., Williams, D., Sauvaud, J.-A., Thocaven, J.-J., Moreau, T., Winningham, D., Frahm, R., Scherrer, J., Sharber, J., Wurz, P., Bochsler, P., 2004. ASPERA-3: Analyzer of space plasmas and energetic ions for Mars Express. In: Wilson, A. (Ed.), Mars Express: The Scientific Payload. ESA Publications Division, Noordwijk, The Netherlands, pp. 121–139. ESA Special Publication SP-1240.

Brecht, S.H., 1997. Hybrid simulations of the magnetic topology of Mars. J. Geophys. Res. 102 (A3), 4743–4750.

C:son Brandt, P., Barabash, S., Roelof, E.C., Chase, C.J., 2001. Energetic neutral atom imaging at low altitudes from the Swedish microsatellite Astrid: Observations at low (⩽10 keV) energies. J. Geophys. Res. 106 (A11), 24663–24674.

Dolginov, S.S., 1978. On the magnetic-field of Mars—Mars-5 evidence. Geophys. Res. Lett. 5 (1), 93–95.

Dolginov, S.S., Yeroskenko, Y.G., Zhuzgov, L.N., 1973. The magnetic field in the very close neighborhood of Mars according to data from the Mars-2 and -3 spacecraft. J. Geophys. Res. 78 (22), 4779–4786.

Futaana, Y., Barabash, S., Grigoriev, A., Holmström, M., Kallio, E., C:son Brandt, P., Gunell, H., Brinkfeld, K., Lundin, R., Andersson, H., Yamauchi, M., McKenna-Lawler, S., Winningham, J.D., Frahm, R.A., Sharber, J.R., Scherrer, J., Coates, A.J., Linder, D.R., Kataria, D.O., Säles, T., Riihela, P., Schmidt, W., Koskinen, H., Kozyra, J., Luhmann, J., Roelof, E., Williams, D., Livi, S., Curtis, C.C., Hsieh, K.C., Sandel, B.R., Grande, M., Carter, M., Sauvaud, J.–A., Fedorov, A., Thocaven, J.–J., Orsini, S., Cerulli-Irelli, R., Maggi, M., Wurz, P., Bochsler, P., Galli, A., Krupp, N., Woch, J., Fränz, M., Asamura, K., Dierker, C., 2006. First ENA observations at Mars: ENA emissions from the martian upper atmosphere. Icarus 182, 424–430.

Holmström, M., Barabash, S., Kallio, E., 2002. Energetic neutral atoms at Mars. 1. Imaging of solar wind protons. J. Geophys. Res. 107 (A10), doi:10.1029/2001JA000325. 1277.

Kallio, E., Barabash, S., 2001. Atmospheric effects of precipitation energetic hydrogen atoms on the martian atmosphere. J. Geophys. Res. 106 (A1), 165–177.

Lichtenegger, H., Lammer, H., Stumptner, W., 2002. Energetic neutral atoms at Mars. 3. Flux and energy distributions of planetary energetic H atoms. J. Geophys. Res. 107 (A10), doi:10.1029/2001JA000322. 1279.

Luhmann, J.G., Bauer, S.J., 1992. Solar wind effects on atmosphere evolution at Venus and Mars. In: Luhmann, J.G., Tatrallyay, M., Pepin, R.O. (Eds.), Venus and Mars: Atmospheres, Ionospheres, and Solar Wind Interaction. Am. Geophys. Union, Washington, DC, pp. 417–430. AGU Geophysical Monograph 66.

Lundin, R., Barabash, S., Andersson, H., Holmström, M., Grigoriev, A., Yamauchi, M., Sauvaud, J.-A., Fedorov, A., Budnik, E., Thocaven, J.-J., Winningham, D., Frahm, R., Scherrer, J., Sharber, J., Asamura, K., Hayakawa, H., Coates, A., Linder, D.R., Curtis, C., Hsieh, K.C., Sandel, B.R., Grande, M., Carter, M., Reading, D.H., Koskinen, H., Kallio, E., Riihela, P., Schmidt, W., Säles, T., Kozyra, J., Krupp, N., Woch, J., Luhmann, J., McKenna-Lawler, S., Cerulli-Irelli, R., Orsini, S., Maggi, M., Mura, A., Milillo, A., Roelof, E., Williams, D., Livi, S., Brandt, P., Wurz, P., Bochsler, P., 2004. Solar wind-induced atmospheric erosion at Mars: First results from ASPERA-3 on Mars Express. Science 305, 1933–1936.

Mauk, B.H., Mitchell, D.G., Krimigis, S.M., Roelof, E.C., Paranicas, C.P., 2003. Energetic neutral atoms from a trans-Europa gas torus at Jupiter. Nature 421, 920–922.

Mitchell, D.G., Jaskulek, S.E., Schlemm, C.E., Keath, E.P., Thompson, R.E., Tossman, B.E., Boldt, J.D., Hayes, J.R., Andrews, G.B., Paschalidis, N., Hamilton, D.C., Lundgren, R.A., Tums, E.O., Wilson IV, P., Voss, H.D., Prentice, D., Hsieh, K.C., Curtis, C.C., Powell, F.R., 2000. High energy neutral atom (HENA) imager for the IMAGE mission. Space Sci. Rev. 91 (1–2), 67–112.

Moore, T.E., Chornay, D.J., Collier, M.R., Herrero, F.A., Johnson, J., Johnson, M.A., Keller, J.W., Laudadio, J.F., Lobell, J.F., Ogilvie, K.W., Rozmarynowski, P., Fuselier, S.A., Ghielmetti, A.G., Hertzberg, E., Hamilton, D.C., Lundgren, R., Wilson, P., Walpole, P., Stephen, T.M., Peko, B.L., Van Zyl, B., Wurz, P., Quinn, J.M., Wilson, G.R., 2000. The low energy neutral atom imager for IMAGE. Space Sci. Rev. 91 (1–2), 155–195.

Mura, A., Milillo, A., Orsini, S., 2002. Energetic neutral atoms at Mars. 2. Imaging of the solar wind–Phobos interaction. J. Geophys. Res. 107 (A10), doi:10.1029/2001JA000328. 1278.

Pollock, C.J., Asamura, K., Baldonado, J., Balkey, M.M., Barker, P., Burch, J.L., Korpela, E.J., Cravens, J., Dirks, G., Fok, M.-C., Funsten, H.O., Grande, M., Gruntman, M., Hanley, J., Jahn, J.-M., Jenkins, M., Lamp-

ton, M., Marckwordt, M., McComas, D.J., Mukai, T., Penegor, G., Pope, S., Ritzau, S., Schattenburg, M.L., Scime, E., Skoug, R., Spurgeon, W., Stecklein, T., Storms, S., Urdiales, C., Valek, P., van Beek, J.T.M., Weidner, S.E., Wüest, M., Young, M.K., Zinsmeyer, C., 2000. Medium energy neutral atom (MENA) imager for the IMAGE mission. Space Sci. Rev. 91 (1–2), 113–154.

Roelof, E.C., Mitchell, D.G., Williams, D.J., 1985. Energetic neutral atoms ($E \sim 50$ keV) from the ring current: IMP 7/8 and ISEE 1. J. Geophys. Res. 90, 10991–11008.

Tanaka, T., Murawski, K., 1997. Three-dimensional MHD simulation of the solar wind interaction with the ionosphere of Venus: Results of two-component reacting plasma simulation. J. Geophys. Res. 102 (A9), 19805–19821.

Terada, N., Machida, S., Shinagawa, H., 2002. Global hybrid simulation of the Kelvin–Helmholtz instability at the Venus ionosphere. J. Geophys. Res. 107 (A12), doi:10.1029/2001JA009224. 1471.

Vignes, D., Mazelle, C., Rème, H., Acuña, M.H., Connerney, J.E.P., Lin, R.P., Mitchell, D.L., Cloutier, P., Crider, D.H., Ness, N.F., 2000. The solar wind interaction with Mars: Locations and shapes of the bow shock and the magnetic pile-up boundary from the observations of the MAG/ER experiment onboard Mars Global Surveyor. Geophys. Res. Lett. 27 (1), 49–52.

Voss, H.D., Mobilia, J., Collin, H.L., Imhof, W.L., 1993. Satellite observations and instrumentation for measuring energetic neutral atoms. Opt. Eng. 32, 3083–3089.